Weather Regimes in the Pacific from a GCM. Part II: Dynamics and Stability

A. HANNACHI

Department of Meteorology, Edinburgh University, Edinburgh, United Kingdom

(Manuscript received 13 June 1995, in final form 2 October 1996)

ABSTRACT

The Pacific weather regimes found by Haines and Hannachi from a GCM perpetual January 10-year run, identified as ±Pacific–North American (PNA), are examined for stability both within a model-derived EOF phase space and the full phase space for the 500-mb flow level. The authors also examine the behavior of the 500-mb streamfunction tendency based on the barotropic vorticity equation model projected onto the EOF phase space. Normal mode and nonnormal mode analysis of these regimes are performed. It is shown in particular that the +PNA state is less stable than the −PNA, which can explain previous results concerning the greater robustness in finding the −PNA state as a fixed point in the attractor. Of particular interest is the local character of the +PNA regime, which indicates fast growth rates within the EOF phase space of the order 3–4 days.

1. Introduction

The impact of weather regimes on the low-frequency variability of the atmosphere is now well known and has been documented during the last decade or so. Although the atmosphere as a whole is not completely predictable beyond about a week due to its chaotic behavior, there are some periods when the predictability can be improved (Mansfield 1986). The observed low-frequency intraseasonal oscillations (10–100 days) (Branstator 1987) and also periods of strong El Niño events during which a strong Pacific–North American (PNA)-like pattern is evident (Quiroz 1983) are examples of such periods. Weather regimes can also be regarded as those large-scale anomalies with recognizable quasi-stationary spatial pattern. During the life time of these patterns the high-frequency disturbances are very often active and contribute in maintaining these structures (Shutts 1983). For example, blocking over Europe has been noticed by Rex (1950) and Namias (1964) to persist for several weeks. The occurrence or nonoccurrence of blocking can determine to a large extent the distinctive character of an individual season (Legras and Ghil 1985), although Kimoto et al. (1992) and Anderson (1992) noticed that blocking tends to be highly unstable and it is not easy to predict its persistence.

Lorenz (1963) was the first to show, using a highly truncated dissipative–advective model, that the atmosphere might possess more than one flow regime with irregular transitions. Charney and DeVore (1979) pioneered the multiequilibria idea in the atmosphere using a simple β-channel model to show how multiple metastable equilibria may arise in a more realistic framework. In an attempt to apply the multiple equilibria idea of Charney and Devore to a more realistic framework, Legras and Ghil (1985) used a full barotropic model on the sphere and obtained regimes through balancing the tendency equation and showed that their equilibria, although unstable, can still intermittently attract the trajectory to spend some time in their neighborhood. Vautard and Legras (1988) studied a baroclinic channel model seeking stationarity on large scales only while small scales were allowed to behave freely. Also, Mukougawa (1988) proposed another technique for searching weather regimes, using a two-layer β-channel quasigeostrophic model, seeking periods where the model tendency is smaller than a prescribed threshold value. Different probabilistic approaches and techniques based on clustering analysis were intensively used (Sutera 1986; Hansen and Sutera 1986; Mo and Ghil 1988; Molteni et al. 1990) to look for multiple equilibria in planetary wave amplitude statistics. Although the previous findings may constitute good support for the existence of persistent and recurrent weather patterns, there are still some controversies (Tung and Rosenthal 1985; Nitshe et al. 1994) that need to be addressed.

The idea of weather regimes as being controlled by intermittently attracting fixed points (Branstator and Opsteegh 1989) was consistently exploited and used within a GCM context by Haines and Hannachi (1995, hereafter referred to as Part I). They looked for quasi-stationarity from a long run of a GCM by minimizing the streamfunction tendency equation within the phase space of the low-pass filtered EOFs, thus improving the

Corresponding author address: Dr. A. Hannachi, Department of Meteorology, University J.C.M.B., Edinburgh EH9 3JZ, United Kingdom.

chance that the solutions lie within the attractor and escaping the trap of free Rossby waves, which constitute a large family of exact solutions of the barotropic vorticity equation. They identified the ±PNA teleconnection patterns of Wallace and Gutzler (1981) as local tendency minima. They showed also, using a multivariate mixture analysis technique, that the model trajectory does indeed spend intermittent periods near two preferred states that look much like these ±PNA dynamical patterns. They, therefore, concluded that these teleconnection patterns may act as attracting fixed points for the model trajectory.

These persistent low-frequency patterns may be excited linearly by resonant external forcing (Tung and Lindzen 1979) or by variation of the tropical sea surface temperature (Hoskins and Karoly 1981) and through nonlinearity by internal atmospheric variability by wave–wave interaction (Egger l978). Simmons et al. (1983, SWB hereafter) obtained a PNA mode as a response to a linearized barotropic model around the 300-mb climatology with localized tropical forcing. Three-dimensional normal mode analyses were used by Frederiksen (1992) to show that PNA is obtained as a mature stage of onset-of-blocking disturbance modes through combined baroclinic–barotropic instability. Palmer (1988) showed that the variability in forecast skill is strongly related to the fluctuations in the PNA mode and suggested that the growth of forecast error is related to the barotropic stability of the regime flow. In particular, he suggested that the variability in skill is related to the sign of the PNA. This has been further discussed by Molteni and Palmer (1993) using normal and nonnormal mode stability studies of large-scale flow patterns. To relate our results to previous findings, we use the dataset of the 10-year perpetual January run described in Part I; we will review the technique and the solutions found there in the light of their stability. A review of the technique and the different solutions found in Part I will be presented in section 2. The stability based on the projected barotropic vorticity tendency onto the EOF phase space will be presented in section 3. Section 4 will contain results of the stability analyses of the solutions performed using both the EOF-based stability analysis and the full spectrum analysis. We will discuss the results in section 5 and conclusions will be given in the last section.

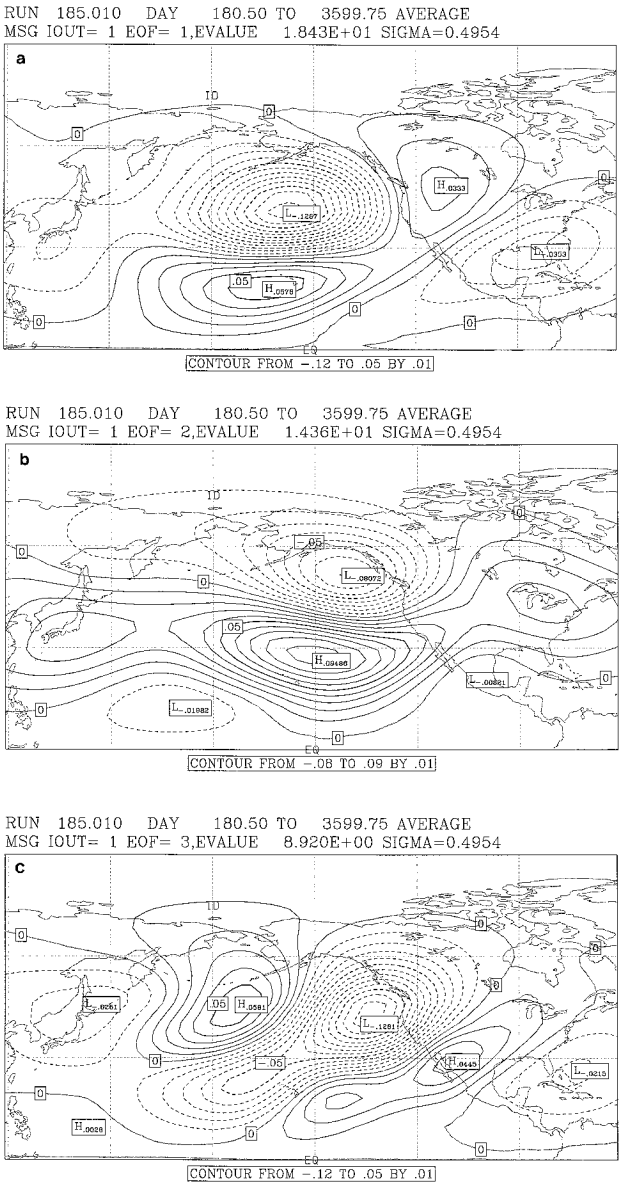

FIG. 1. Pacific 5-day low pass EOFs with their percentage variances, (a) EOF1 with 18.4%, (b) EOF2 with 14.4%, and (c) EOF3 with 8.9%. Contour interval arbitrary, negative values dashed.

2. Flow regimes in the GCM

a. Low frequency and quasi stationarity in the GCM

This study uses a 10-year perpetual January run of the U.K. Universities Global Atmospheric Modelling Project (UGAMP) GCM using a Betts–Miller convection scheme, as described in Part I (and references therein), with T42 horizontal resolution and 19 vertical levels. The analyzed dataset consists of the 500-mb streamfunction and is sampled every 3/4 day. The Northern Hemisphere (NH) time mean flow (Fig. 2 of Part I) shows a pronounced streamfunction variability in the Pacific and Atlantic jets regions. In Part I the 5-day low-pass Lanczos filter EOFs over the Northern Hemisphere and over the Pacific area were derived, and it was shown, particularly, that the first EOF exhibits a PNA signature while the following one is more related to the latitudinal variability in the stormtrack positions. The EOFs for the Pacific sector show more clearly the preceding signature (Fig. 1) and explain more variance with the first three explaining around 42% of the low-frequency variability. To look for quasi-stationary states, we used the phase space spanned by the first few significant EOFs and

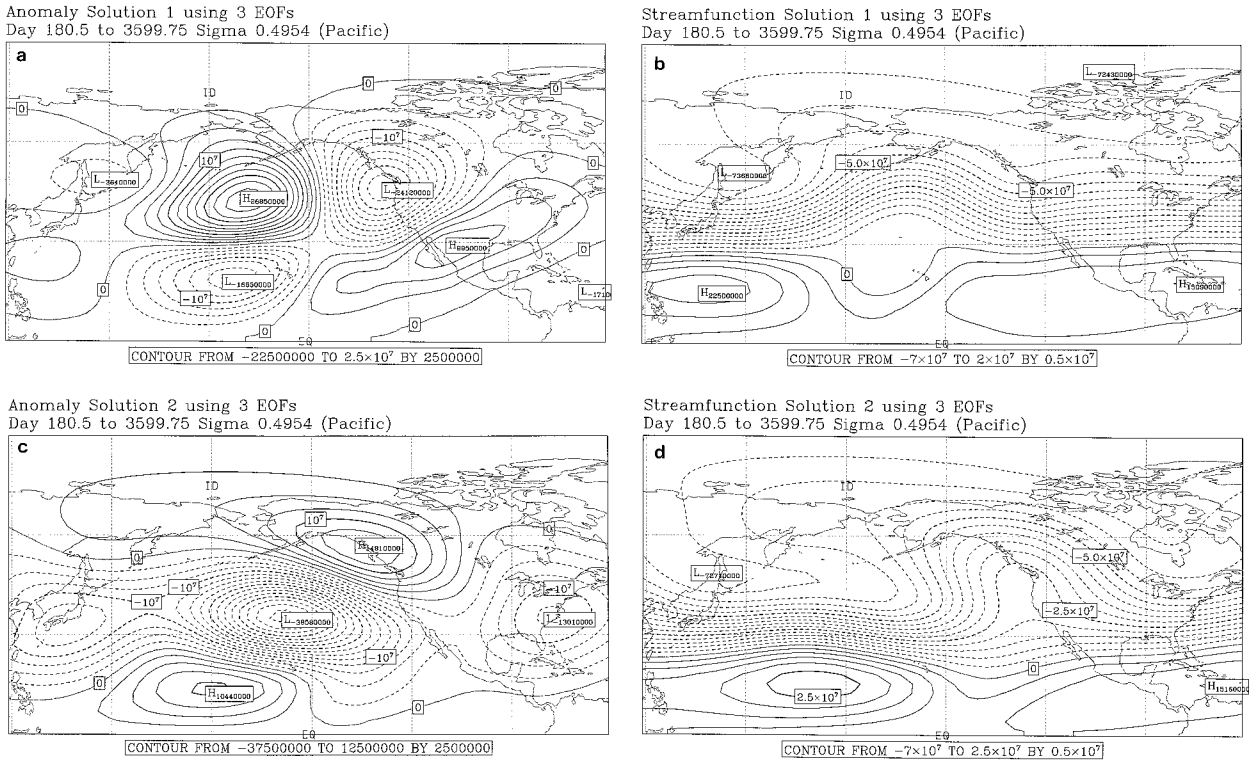

FIG. 2. Solutions with three EOFs minimizing the tendency I over the Pacific. (a) −PNA anomaly, (b) climatology −PNA, (c) +PNA anomaly, and (d) climatology +PNA. Contour interval in (a) and (c) is 2.5×10^6 m^2 s^{-1} and is 5×10^6 m^2 s^{-1} in (b) and (d). Negative values are dashed.

minimized the streamfunction tendency calculated from the barotropic vorticity equation. If we designate by ψ_i the ith EOF and $\bar{\psi}$ the mean flow streamfunction, then the streamfunction at each point in the phase space can be written as

$$\psi = \bar{\psi} + \sum_{i=1}^{d} a_i \psi_i, \tag{1}$$

where d is the phase space dimension. The streamfunction tendency based on the barotropic vorticity equation is

$$\frac{\partial \psi}{\partial t} = -\nabla^{-2}[J(\psi, \zeta_a)], \tag{2}$$

where $\zeta_a = \nabla^2\psi + f$ is the absolute vorticity, f being the planetary vorticity. We thus look for locations in the phase space that minimize the average ψ tendency,

$$I = \int_A \left(\frac{\partial \psi}{\partial t}\right)^2 dA, \tag{3}$$

over the area of concern A.

Two minima identified as ±PNA were found over the Pacific (Fig. 2) (for more detail see Part I). The procedure was also extended to the whole NH and again two minima were found. The first one has a +PNA signature over the Pacific with an east Atlantic pattern dominant in the Atlantic, while the other shows a −PNA signature with an associated west Atlantic pattern (see Fig. 12 of Part I). Further analyses of the robustness of these solutions to the number of degrees of freedom and the role of eddies is briefly described in the next section.

b. Robustness of the solutions and role of the eddies

Dynamical analysis of the EOF phase space reveals inhomogeneities in the streamfunction tendency, which as Part I showed can affect the model trajectory. The structure of the solutions is, to some extent, related to the robustness of the spatial regions that do not seem to change too much when changing, for example, the number of EOF degrees of freedom or by including the role of the eddies as below.

When the EOF phase space dimension increases, the average streamfunction tendency (cost function) decreases, showing that when the number of degrees of freedom increases, the tendency in the phase space can tend to zero in the limit when the whole spectrum is considered since exact barotropic Rossby–Haurwitz waves may be found (there is no explicit external forcing such as topographic or thermal driving in our barotropic model).

When, in Part I, we extended the technique to the whole NH, we noticed that the mean vorticity advection at 500 mb (Fig. 3a) is clearly dominated by the Tibetan

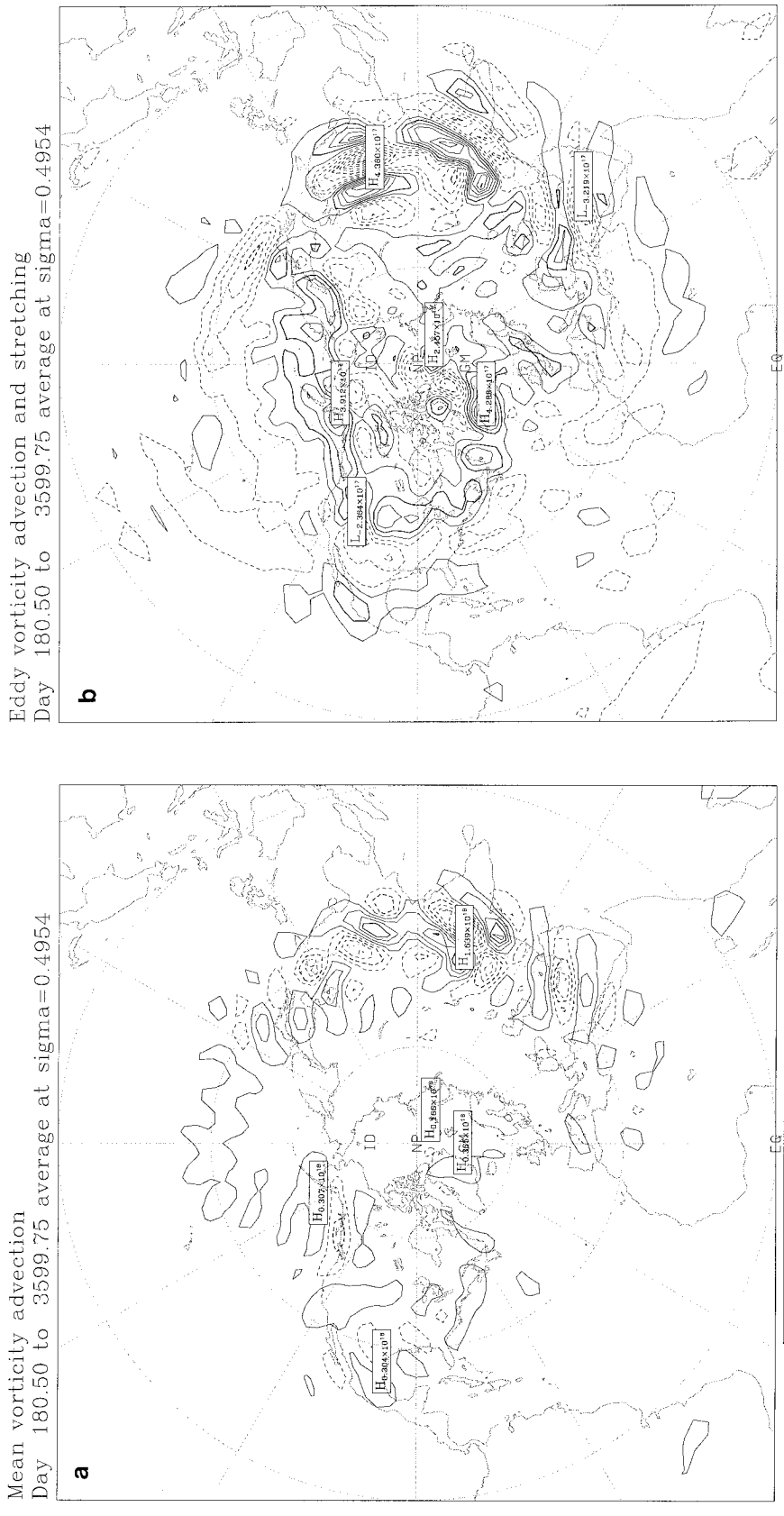

FIG. 3. Mean vorticity advection (a) and mean eddy vorticity advection plus stretching at 500 mb. Contour interval is 1.19×10^{-10} s^{-1} in (a) and 3×10^{-11} s^{-1} in (b). The field in (b) is multiplied by −1.

high, which results from the advection of the mean vorticity by the mean flow $J(\overline{\psi}, \Delta\overline{\psi})$. To help reduce this effect, the latter term has been replaced by its eddy counterpart following the vorticity budget equation

$$0 = J(\overline{\psi}, \overline{\zeta}) + \overline{J(\psi', \zeta')} + \overline{\zeta' D'} + R, \qquad (4)$$

where the dash is for the perturbation from the time mean flow, D stands for the divergence term, and R contains the remaining, primarily mean flow, residual terms, for example, mean vorticity stretching, vertical vorticity advection, and other terms related to the coordinate transform. As a first approximation, we consider that R does not change with the regime changes, compared to the other terms, and then we look for a small vorticity displacement, ζ_r, from the mean flow that minimizes the average streamfunction residual tendency (see Part I for more detail):

$$I' = \int_A [\nabla^{-2}(J(\overline{\psi}, \zeta_r) + J(\psi_r, \overline{\zeta_a}) + J(\psi_r, \zeta_r) - \overline{J(\psi', \zeta')} - \overline{\zeta' D'})]^2 \, dA, \qquad (5)$$

where $\psi_r = \psi - \overline{\psi} = \nabla^{-2}\zeta_r$ is the streamfunction anomaly. Here, I' is obtained similarly to I except that the mean vorticity advection by the mean flow is replaced by its eddy counterpart following the approximation

$$J(\overline{\psi}, \overline{\zeta}) = -\overline{J(\psi', \zeta')} - \overline{\zeta' D'}$$

deduced from (4). By including the role of the eddies the large terms in the mean vorticity advection over the Tibetan plateau, for example, were reduced (Fig. 3b). Again, two solutions (±PNA) were found for the Pacific case and also for the Northern Hemisphere case (see Figs. 11 and 12 of Part I). The structure of the new solutions does not differ too much from the previous ones. That the solutions do not seem to change much when adding more EOFs or including the role of the eddies and that the cost function at the regimes can change is in agreement with the conclusion made by Molteni et al. (1993) concerning the position and the populations of the regimes in phase space. They showed, using a modified Lorenz system where they added a linear forcing to the original Lorenz system (Lorenz 1963), that within the range of reasonably varying forcing, the positions of the two regimes of the model are generally fixed but the populations of these regimes can be biased toward one of them.

3. The flow of the model trajectory and the barotropic vorticity equation

The technique described in Part I seeks dynamical and statistical regimes using, respectively, the barotropic vorticity equation and the model trajectory. It supposes implicitly that the projected dynamics of the model trajectory and the barotropic vorticity equation, respectively, onto the EOF phase space are comparable. Ideally this is the case for large-scale flows; however, in practice, they are different because the projected GCM trajectory onto the EOF phase space is chaotic and generally more irregular due to the high dimension of the GCM attractor. The flow induced by the barotropic vorticity equation projected onto the same phase space is smoother and generally more regular. For a given d-dimensional EOF phase space where the flow ψ and its absolute vorticity ζ_a are given by

$$\psi = \overline{\psi} + \sum_{k=1}^{d} X_k \psi_k, \; \zeta_a = \Delta\psi + f,$$

the flow deduced from the barotropic vorticity equation is the vector field of the following d-dimensional dynamical system:

$$\frac{dX}{dt} = F(X) \qquad (6)$$

with

$$X = (X_1, \ldots, X_d), \quad \text{and} \quad F(X) = (F_1(X), \ldots, F_d(X))$$

and

$$F_k(X) = \frac{\langle -\nabla^{-2} J(\psi, \zeta_a), \psi_k \rangle}{\langle \psi_k, \psi_k \rangle}, \qquad (7)$$

where $\langle , \rangle$ is a real scalar product. When the residual tendency is calculated by compensating for the eddies in the mean vorticity budget (4), one has to replace the vorticity advection $J(\psi, \zeta_a)$ by the following residual tendency J' as used in Eq. (5):

$$J' = J(\overline{\psi}, \zeta_r) + J(\psi_r, \overline{\zeta_a}) + J(\psi_r, \zeta_r) - \overline{J(\psi', \zeta')} - \overline{\zeta' D'}, \qquad (8)$$

and the corresponding projected tendency

$$\frac{dX}{dt} = F'(X)$$

in this case takes the form

$$F'_k(X) = \frac{\langle -\nabla^{-2} J', \psi_k \rangle}{\langle \psi_k, \psi_k \rangle}.$$

In what follows, we will focus on the dynamical solutions that minimize I and the resulting projected tendency (6) and (7). The projected tendency based on Eq. (7) is shown in Fig. 4 within the first two Pacific EOFs. In this figure, the dots show the projection of the dynamical solutions, which minimize I of (3), obtained within the first three Pacific EOFs phase space (Table 1). As can be seen, the flow is smooth and regular with two locations of singular points. One of them, which has a positive first EOF component, shows an unstable node and its location coincides well with the projection of one minimum (+PNA for instance). The other center, which has a negative first component and is farther away from the origin, looks more like a stable node with converging tendency vectors. Its position does not coincide with the second minimum (−PNA). In fact, this

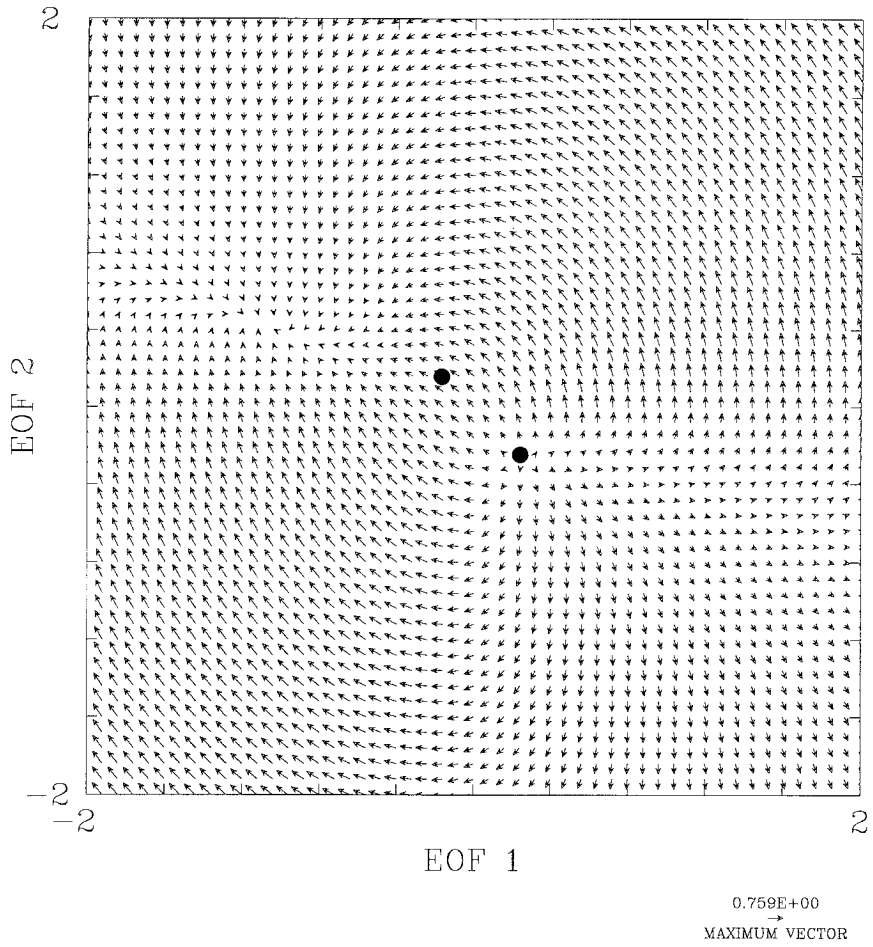

FIG. 4. The flow of the barotropic vorticity equation projected onto the first two Pacific EOFs phase space. The dots indicate the projection of the dynamical solutions in Table 1 obtained with the first three Pacific EOFs.

latter center is closer to the origin than the singular point of the flow, which is farther away from it and is not within the range of commonly observed amplitudes. That the location of the −PNA pattern does not project onto a singular point is not surprising. In fact, the minimum set of EOFs needed to obtain the two regimes is composed of the first three EOFs. Within the first two EOFs only the +PNA regime, which projects well onto the singular point, is obtained. The third EOF is indeed necessary to obtain the −PNA pattern (see its amplitude following EOF3 in Table 1). The mismatch between the flow regimes and the singular points will be addressed in more detail in a subsequent paper. Although the two minima are not exact free modes, nevertheless they still

TABLE 1. EOF amplitudes of the dynamical quasi-stationary states along with the *e*-folding times and periods (in days) of their barotropically most unstable normal modes for different Pacific EOF phase space dimensions at T42 and T21 resolutions. The period ∞ indicates that the mode is stationary; that is, it grows exponentially without phase changes.

3–6 EOF solution	Solution amplitudes						*e*-folding times		Periods	
	α_1	α_2	α_3	α_4	α_5	α_6	T42	T21	T42	T21
−PNA	−.158	.055	.187				19.2	20.4	155.6	189.5
+PNA	.211	−.253	.038				10.1	9.4	10.7	12.3
−PNA	−.240	.071	.199	−.169			12.5	13.5	498.4	209.1
+PNA	.217	−.262	.053	−.049			7.0	6.1	∞	∞
−PNA	−.217	−.021	.136	−.106	.180		11.4	8.8	∞	∞
+PNA	.144	−.299	−.037	−.021	.128		11.1	7.7	10.9	91.6
−PNA	−.214	.012	.101	−.115	.219	.083	9.6	9.0	∞	∞
+PNA	.099	−.306	−.084	−.005	.170	.100	6.1	5.6	∞	∞

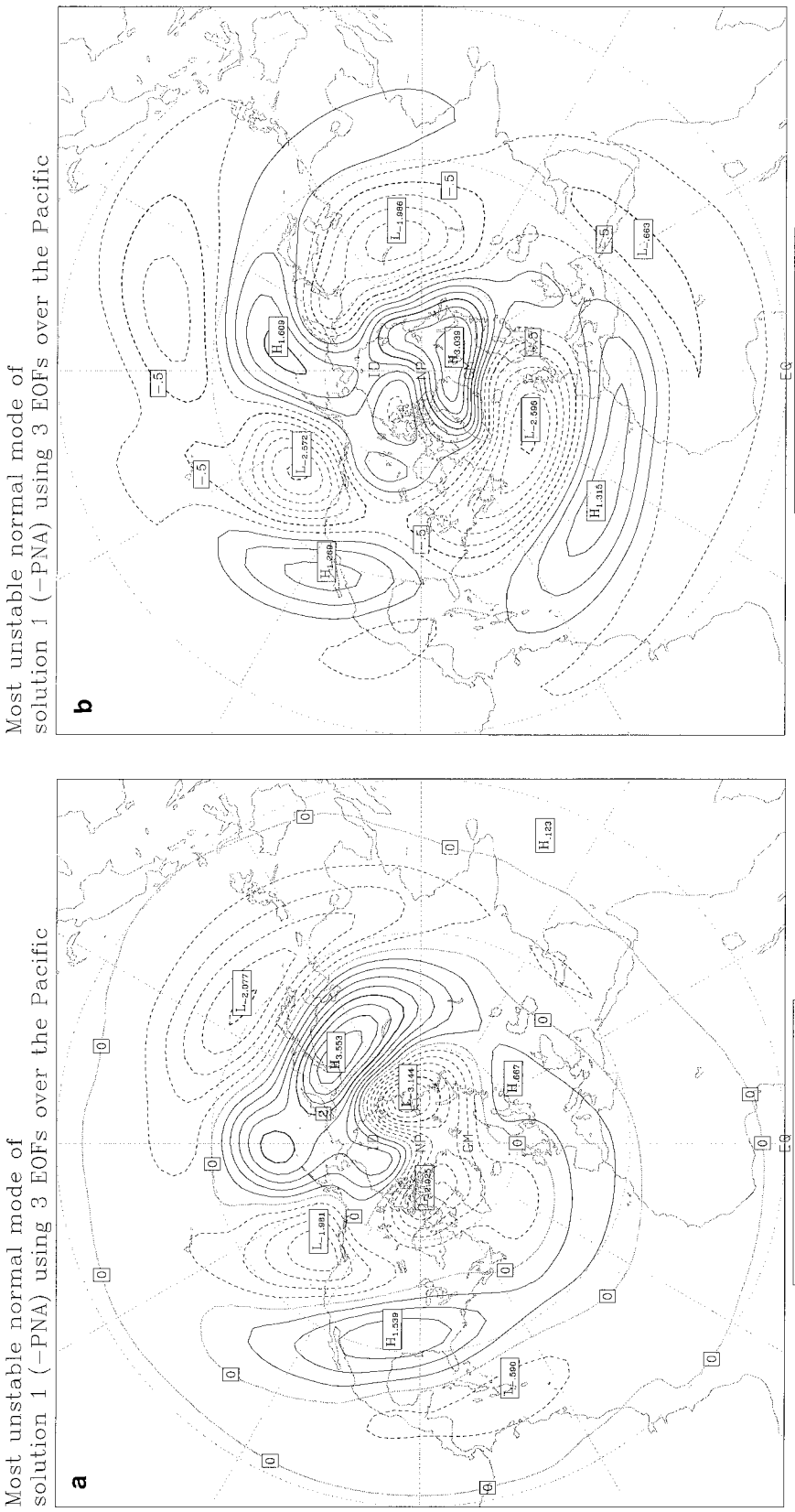

FIG. 5. The most unstable normal modes for the −PNA pattern [(a), (b)] (real and imaginary parts, respectively) and for the +PNA pattern [(c), (d)]. Contour interval is arbitrary, negative values are dashed.

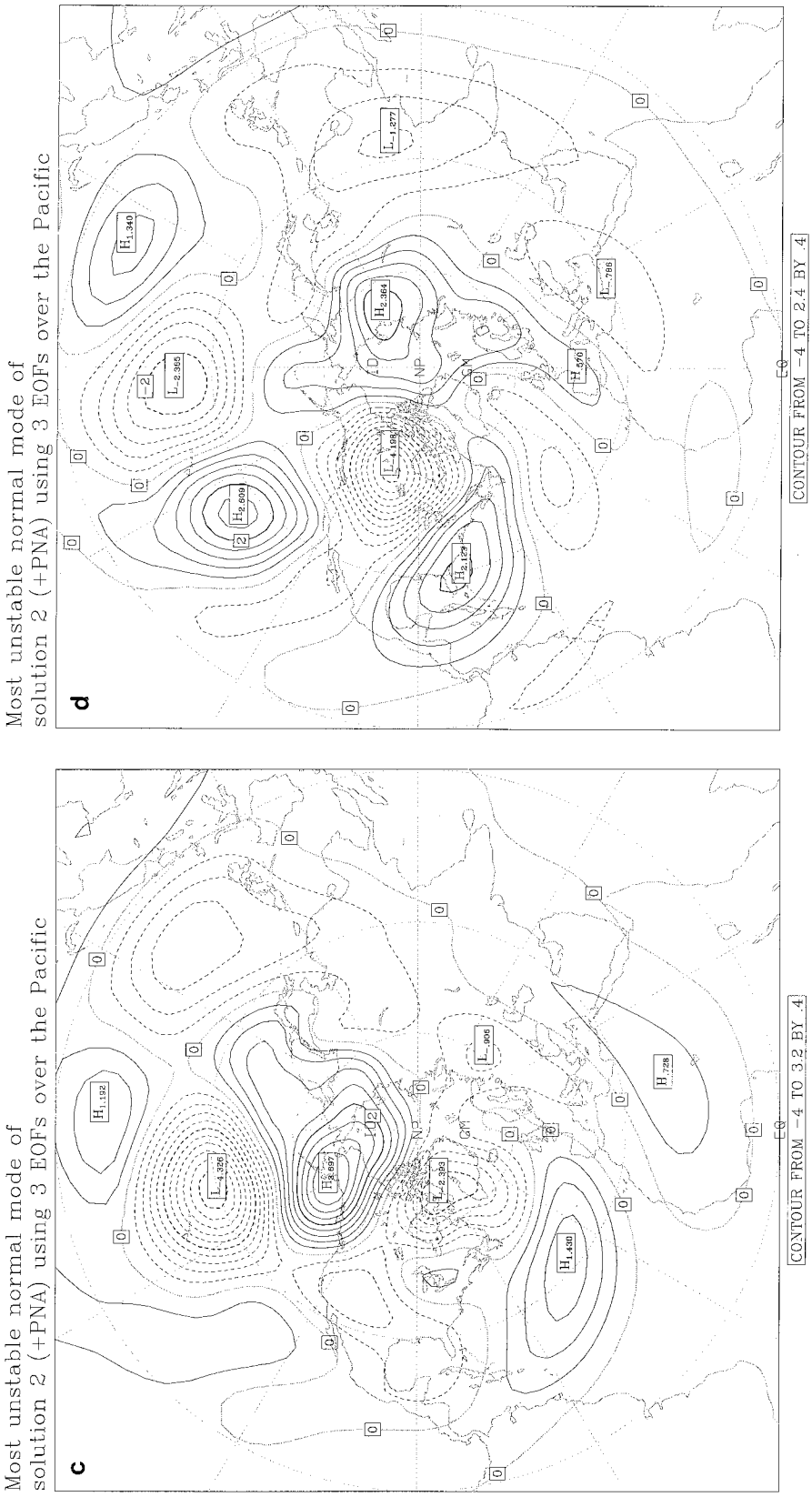

FIG. 5. *(Continued)*

minimize the streamfunction tendency so that one can consider their normal mode stability (see Andrews 1984). At first sight, Fig. 4 shows only one direction of transition, that is, from the +PNA regime to the −PNA regime. This suggests that the +PNA solution may be less stable than the −PNA, and a linear stability analysis using normal modes and nonnormal modes will be presented in the next section supporting this suggestion.

4. Stability analysis of the flow regimes

a. Normal mode stability

Diagrams of tendency vectors within a reduced EOF phase space, such as Fig. 4, are useful in studying the structure of the flow and looking, for example, for oscillations of the model. Recently, James et al. (1994), seeking to understand the wave–zonal flow interaction and the ultralow-frequency variability in GCMs, integrated a simplified global circulation model (SGCM), without physics and with a perpetual solstice boundary condition. They used a similar representation of the flow with the first two zonal-mean zonal wind EOFs, which describe the adjustments of the zonal jet due to baroclinic wave growth and decay. They showed that for a series of single wave life cycles such an adjustment can be represented by a circuit within the EOF phase space, with cumulative timescale of about 150 days. On the other hand, Branstator (1995) showed that the storm-track is controlled by the time-mean flow and that the barotropic component of the low-frequency disturbances has a large impact on the high-frequency disturbances. The results of SWB suggested, based on the work of Hoskins et al. (1983), that much of the low-frequency variability in the Northern Hemisphere winter could be associated with disturbances that derive their energy from the basic state through barotropic instability. Borges and Sardeshmukh (1995) have recently suggested that, with realistic frictional parameters, most observed large-scale time-mean flows would not be barotropically unstable. Here we investigate whether barotropic instability could explain some features of the modeled flow regimes from the preceding sections.

We investigate here the stability properties of the quasi-stationary states presented in section 2. The calculation of the most unstable modes is performed using solutions of an eigenvalue problem of the linearized barotropic vorticity equation, as in SWB, and is also performed for the linearized tendency equation of the streamfunction projected onto the EOF phase space as in Eq. (6). The main aim is to compare the stability of the +PNA and −PNA regimes using both the full barotropic vorticity equation and its projection onto the EOF phase space. These PNA regime centers are not exact free modes, but they minimize the average barotropic streamfunction tendency and they probably lie on the model attractor (because of the use of the EOF phase space). To allow this stability analysis, one has to suppose the existence of constant forcing terms on the rhs of Eq. (2) or Eq. (6) that make these regimes stationary states (see Andrews 1984 for attendent dangers).

The linearized barotropic vorticity equation with a basic state, ψ_b, is written as

$$\frac{\partial \zeta'}{\partial t} = -J(\psi_b, \zeta') - J(\psi', \zeta_b) - \eta\nabla^4\zeta', \qquad (9)$$

where $\zeta_b = \Delta\psi_b + f$ is the basic-state absolute vorticity, $\zeta' = \Delta\psi'$ is the perturbation vorticity, and η is a diffusion coefficient fixed to 2×10^{16} m^4 s^{-1}. The normal mode solutions take the form $\zeta' = \mathrm{Re}\{\zeta e^{-i\Omega t}\}$. The linear fourth-order term appearing in (9) is included to damp out the smaller scales at the T42 resolution (see SWB for more detail about the sensitivity to the diffusion coefficient).

The calculation of the most unstable modes is performed using solutions based on different dimensions of the EOF phase space but using the full vorticity equation for the normal modes. In Table 1, we present the *e*-folding times and the periods of the most unstable normal modes of the various quasi-stationary solutions over the Pacific. Figure 5 shows, for $d = 3$, the pattern of the most unstable normal modes of the quasi-stationary patterns ±PNA (Fig. 2). The same stability analysis is performed by changing the spectral resolution where the previous solutions (Fig. 2) were truncated at T21. Table 1 also indicates robustness to variations in the resolution. It shows that the dimension of the phase space does change the phase of the mode. For example, as the dimension increases, the modes tend to become stationary and then grow exponentially. The *e*-folding times do change with the dimension and sometimes double the amplitude (−PNA with three and six EOFs at T42), but a close examination of this change (Fig. 6) reveals that, although the convergence is not straightforward, the *e*-folding times of +PNA and −PNA seem to vary approximately around 8 and 12 days respectively with a more likely convergence for the −PNA pattern. Verkley (1989) and Neven (1993), studying the linear stability of modons, found similar diagrams with an average *e*-folding time of 4–5 days for localized modons with a poor convergence even at high resolution. If one wants to increase indefinitely the phase space dimension in order to obtain convergence, then the small scales will hinder the large-scale quasi-stationary states as these small scales are generally active during the quasi-stationary events (Shutts 1983). Figure 6 shows, also, that the *e*-folding times of the +PNA are smaller than those of the −PNA.

The same analysis is performed, this time, using the linearized tendency equation (6) of the streamfunction within the EOF phase space for the same solutions. Table 2 shows the results for the same patterns as Table 1 but using the projected dynamics. A blank indicates that all the eigenvalues of the corresponding pattern

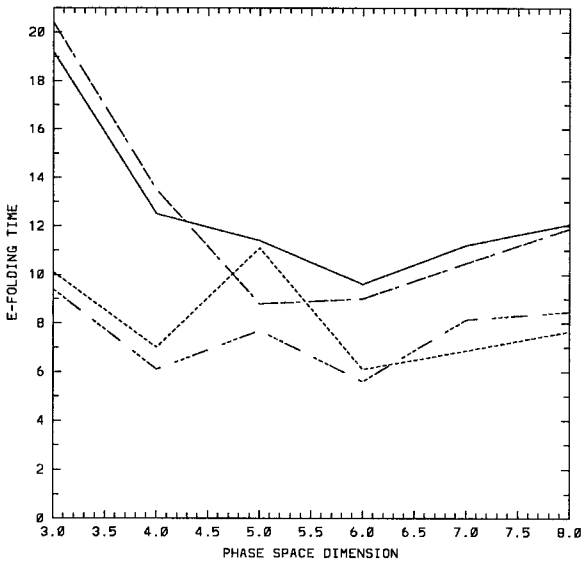

FIG. 6. Variation of the spectrum-based *e*-folding times (days) of the most unstable normal mode with the phase space dimension. The two upper curves are for the −PNA at T42 (continuous) and T21 (dashed) and the two bottom curves are for the +PNA at T42 (dotted) and T21 (dashed).

have negative real parts and are consequently stable. It is seen that the characteristics of the most unstable modes of Table 2 are qualitatively similar to those in Table 1. It can also be seen that the *e*-folding times of the −PNA pattern are larger than those of the +PNA pattern (in agreement with the flow tendencies in Fig. 4). These results show that the projected dynamics may contain important characteristics, and it may be possible to use this simplified system in order to gain some insight into the dynamical characteristics of the model behavior such as the linear growth rates of the regimes, transition diagrams between them, and the time durations for these transitions. For a given possible transition path from one regime to another, as from +PNA to −PNA in Fig. 4 for example, one can find and follow several configurations of the flow that help us to understand the transition process within the model phase space. These transitions between regimes, generally associated with the nonlinearity of the atmospheric system and not requiring changes to external forcing, have small atmospheric predictability (Palmer and Anderson 1994). Understanding and following the path of a transition can address this predictability problem. The time duration for a transition can be obtained by integrating system (6). For example, the transition time from the +PNA to the −PNA regime shown in Fig. 4 is found to be about 37 days. Such a long period includes the mean residence time of the regimes since it starts from the time when the first regime is fully developed and lasts till the next regime is well established. The experiments carried out here show that the −PNA pattern is more stable than the +PNA where our definition of stability is based on normal mode growth. Although,

TABLE 2. The *e*-folding times and periods (days) of the patterns of Table 1, as revealed by the dynamics within the EOF phase space.

EOF phase space dimension	*e*-folding times		Periods	
d	−PNA	+PNA	−PNA	+PNA
3	12.9	2.7	∞	∞
4	—	2.8	—	∞
5	29.4	3.4	14.2	∞
6	13.7	3.6	13.5	∞

qualitatively, there is agreement between the spectrum-based stability analysis and the EOF-based one, growth rates within the reduced space are fast, especially for the +PNA. This point and some others are addressed in the next discussion section.

b. Nonnormal mode stability

In order to further pursue the dynamics within the EOF phase space to allow comparison with Palmer (1988) or Molteni and Palmer (1993), for example, a nonnormal mode analysis of the patterns is carried out within the reduced phase space for simplicity. Singular vector analysis (see below) of the dynamical regimes were performed using the simplified dynamical system (6) in order to give a measure of the finite time instability of the regimes. This is related to the growth rate of small initial perturbations imposed upon a basic-state flow. Lorenz (1965) showed, using a 28-variable model, that the time required for small error perturbations, analogous to observational errors in the atmosphere, to become large is strongly related to the basic circulation pattern and that it varies from a few days to a few weeks.

For a given dynamical system, $\dot{X} = F(X)$, such as (6), any small perturbation δX superimposed upon a trajectory $X_0(t)$ (basic state) at some initial time t_0, will evolve according to the following tangent linear equation of the dynamical system in the vicinity of the basic state $X_0(t)$:

$$\frac{d\delta X}{dt} = \frac{\partial F}{\partial X}(X_0(t))\delta X. \tag{10}$$

Equation (10) describes, to first order, the temporal evolution of the perturbation δX whose solution at time t_1, $\delta X(t_1)$, can be written as

$$\delta X(t_1) = A(t_0, t_1)\delta X(t_0), \tag{11}$$

where A is a linear operator, usually called the resolvent of the system (10). The singular vector analysis is then based on the spectrum of the self adjoint operator $A^*(t_0, t_1)A(t_0, t_1)$, where A^* is the adjoint of the operator A. If $\lambda^2_{\max}$ is the largest eigenvalue of $A^*(t_0, t_1)A(t_0, t_1)$, then $\lambda_{\max}$, which is defined as the largest singular value of the operator $A(t_0, t_1)$, gives a measure of predictability over the finite period of time $[t_0, t_1]$ (e.g., see Lorenz 1965; Molteni and Palmer 1993). Some properties of

TABLE 3. Singular values of the dynamical states represented in Table 1 for different periods of integration as revealed by the dynamics within the EOF phase space. The − and + stand for −PNA and +PNA, respectively.

	½ day		1 day		2 days		4 days		8 days	
d	−	+	−	+	−	+	−	+	−	+
3	1.11	1.45	1.24	2.11	1.53	4.45	2.3	19.84	4.74	393.3
4	1.08	1.46	1.17	2.12	1.35	4.51	1.63	19.93	1.53	362.0
5	1.14	1.58	1.3	2.49	1.68	6.0	2.5	30.0	3.36	424.6
6	1.45	1.68	2.09	2.79	4.15	7.35	12.75	39.44	45.88	478.38

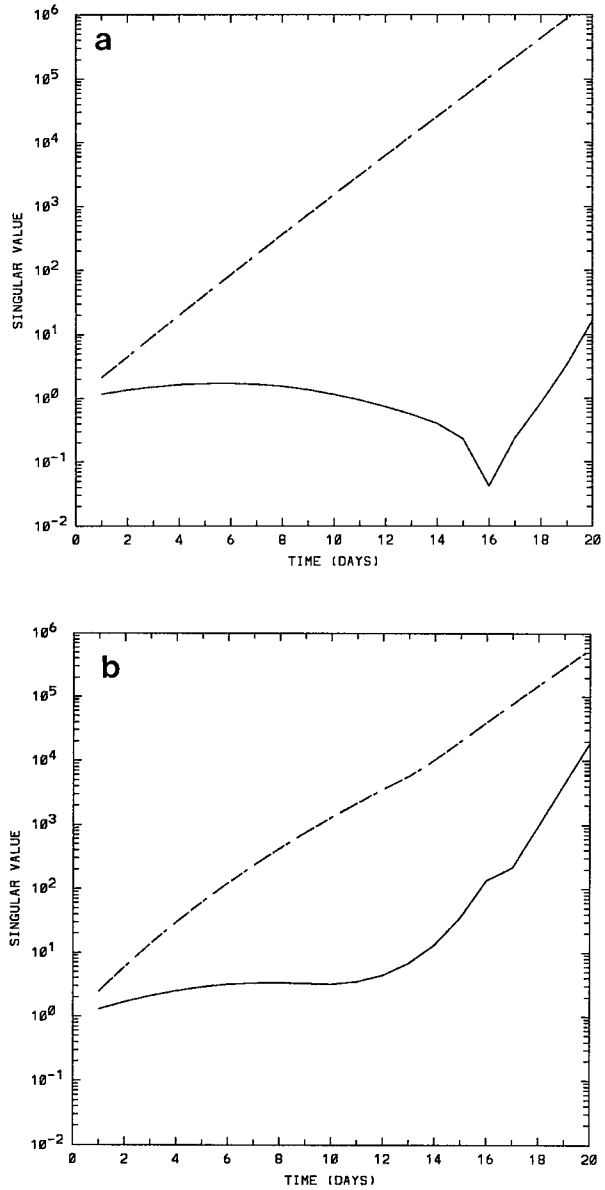

FIG. 7. Variation of the singular values of the ±PNA patterns vs time period of integration using four EOFs (a) and five EOFs (b). Solid line is for the −PNA pattern, dashed line is for the +PNA pattern.

the attractor of a dynamical system can be characterized by the logarithm of the corresponding singular values, when $t_1 \to \infty$, also called the Lyapunov exponents (see Lorenz 1985). The resolvant $A(t_0, t_1)$ of (11) can be approximated by

$$\exp(\partial F/\partial X(t_1 - t_0))$$

if the Jacobian $\partial F/\partial X$ from (10) for the basic state does not vary too much between t_0 and t_1. Table 3 shows the approximated singular values, λ_{max}, for the flow patterns of Table 1 for different periods of integration and different phase space dimensions. Again, from this table one can see that the singular values for +PNA are larger than those for −PNA.

To see more clearly the variation of the singular values with the time integration periods, we show in Fig. 7 the singular values plotted against the time integration periods using four EOFs (Fig. 7a) and five EOFs (Fig. 7b) respectively. They show exponential (Fig. 7a) and nearly exponential (Fig. 7b) growths of the singular values of the +PNA pattern, while the −PNA pattern shows a decrease of its singular value for periods between 13 and 16 days. It is perhaps possible to increase the predictability of this pattern for a period of about 2 weeks as the singular values continue to decrease during the first 2 weeks. This needs, of course, further investigation and more objective analyses of observed data to reach a decisive conclusion. The results of this section help explain why the −PNA dynamical states are more robust to changes in phase space dimension (lower average streamfunction tendency) than the +PNA states (see Tables 1 and 3 of Part I).

5. Discussion

Recurrent and persistent atmospheric patterns can be global or regional. Patterns, such as those associated with some phases of ENSO, are known to be global (Rasmusson and Wallace 1983) while blocking, for example, generally has local character (Dole and Gordon 1983). These different characteristics imply different stability properties of the flow regimes. SWB found a barotropic *e*-folding time of the 300-mb climatological January mean flow of the order 5–10 days. Verkley (1989) and Neven (1993) examined the linear stability of Rossby–Haurwitz waves and localized modons, considered as a prototype of blocking, and found *e*-folding times of the fastest growing disturbance of the order of

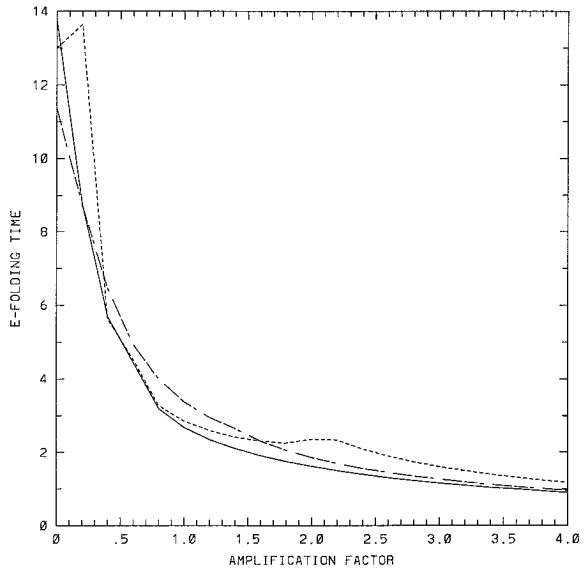

FIG. 8. The *e*-folding time (days) of the most unstable normal mode, based on the reduced dynamics within the phase space, of the +PNA for three (continuous), four (dotted), and five (dashed) EOFs as a function of the amplification factor. The *e*-folding times of the climatology and the dynamical solution can be read for values 0 and 1 of the amplification factor, respectively.

9 and 4–5 days, respectively. Frederiksen and Bell (1990) examined the stability properties of the January 1979 flow at 500 and 300 mb for the period between 10 and 30 January, during which a persistent blocking occurred in the North Atlantic region. They found an *e*-folding time of the fastest growing barotropic mode of the order of 2 and 1.4 days, on average, for the 500-mb and 300-mb levels, respectively. Furthermore, the *e*-folding time went as short as 1.4 and 0.8 days for the same levels on 21 January (see their Fig. 12). The blocking configuration, although unstable, can still constitute one of the recurrent and persistent flows through attracting the phase space trajectory to spend, intermittently, some time in the neighborhood of these unstable equilibria; see, for example, Legras and Ghil (1985) or Lorenz (1963).

The ±PNA regimes (Fig. 2) have different character where the +PNA has a large wave amplitude and is more localized than the −PNA and bears some resemblance to blocking (Fig. 2d). We assert, within this context, that these two characteristics (wave amplitude and localized structure) control the stability of the pattern. To test this hypothesis, the ±PNA anomaly patterns (Figs. 2a,c) were scaled by an amplification factor, α, and a linear stability analysis of the resulting flows performed. Figure 8 shows the resulting *e*-folding times of the fastest growing mode of the +PNA for three, four, and five EOFs using the reduced dynamics (6) for different values of the amplification factor α. In this figure, the growth rate is almost a monotonic (power law) function of the amplification factor. With four EOFs one can see a slight increase of the stability for an amplification

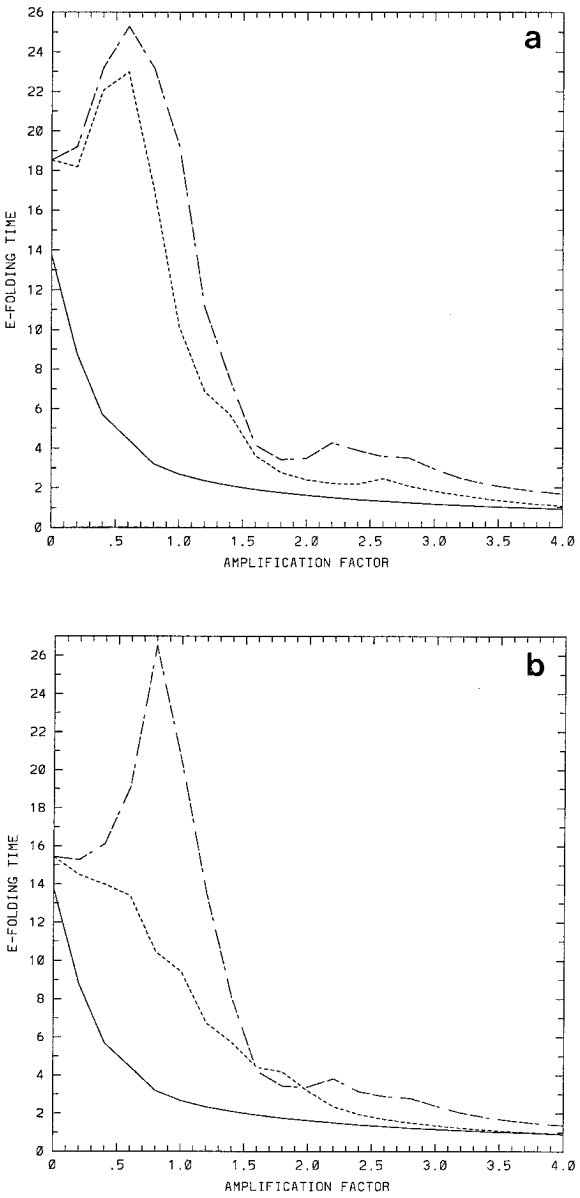

FIG. 9. Same as Fig. 8 but for the spectrum-based normal mode analysis for −PNA (dashed) and +PNA (dotted) at T42 (a) and T21 (b). Also shown, for comparison, is the *e*-folding time of the +PNA based on the reduced space dynamics analysis at three EOFs (continuous).

factor $\alpha = 0.4$. This is not the same for the −PNA where, for increasing α up to the order 1.8, the *e*-folding time increases with wave amplitude (not shown), after which all the real parts of the eigenvalues become eventually negative. The same analysis is performed using the linearized baratropic vorticity equation (9) (Fig. 9) at two resolutions, T42 (Fig. 9a) and T21 (Fig. 9b). One can see from this figure the initial increase of the stability for −PNA at both resolutions while only at T42 for +PNA, after which the *e*-folding time decreases until eventually it converges toward the one obtained

from the reduced dynamics (Fig. 8), always with a smaller growth for the −PNA. This analysis shows that for moderately high wave amplitude (around 1.5 times the observed amplitudes) the simplified dynamics within the reduced phase space can reproduce quite well the growth rates, especially for the +PNA.

The two regimes studied above are quasi-stationary; that is, they minimize the streamfunction tendency. However, the corresponding persistent states, that is, the statistical regimes found in Part I, have weaker wave amplitudes (see Fig. 10 of Part I) and consequently are more stable than the dynamical states. In fact, the statistical −PNA and +PNA regimes (Part I) have an *e*-folding time of their most unstable normal mode, within the reduced phase space, of the order 14 and 9 days, respectively. The latter corresponds to an amplification factor (Fig. 8) of the order 0.2. The ratio between the wave amplitudes of the statistical (Part I) and dynamical (Fig. 2) states is of the order 0.35. The difference between these two ratios is mainly related to the fact that the statistical and dynamical regimes are not completely aligned with the origin. Within the phase space, quasi-stationary regimes and persistent or recurrent regimes are not, necessarily, exactly the same although they are similar or close to each other. Part I discusses the possible causes of the difference between the dynamical and statistical states.

Molteni and Palmer (1993) performed a singular vector analysis on regime centroids and calculated the amplification factor relative to the initial amplitude of the most unstable normal mode and optimal singular vector. The dataset used in their study was composed of filtered fields of 500-mb height covering 32 DJF winters from 1952–1983 taken from ECMWF analyses. They found that the amplification factor of the normal mode of their cluster 2, which is the equivalent of our +PNA-like pattern, is not very different from that of cluster 5, the equivalent of our −PNA pattern, but that the amplification factor of the singular vectors, which is related more to the predictability, is greater for cluster 2 than for cluster 5 until day 4 of the integration for the barotropic model and until day 8 for the baroclinic model. The T21 barotropic vorticity equation model they used, which integrates a prognostic equation for the 300-mb relative vorticity, has got a vorticity damping with timescale of 10 days and a strongly scale-selective horizontal hyperdiffusion with coefficient fixed to about 3.4×10^{38} m^8 s^{-1}. This strong scale selection is not used in our model. Also, when studying medium and extended range predictability of the PNA pattern, Palmer (1988), using a dataset composed of 500 10-day wintertime forecasts of 500-mb height from the ECMWF forecast system (1980/1981 to 1984/1985), found that the growth of an initial perturbation in a linearized barotropic model depended strongly on the sign of the PNA index of the basic flow and that the medium range forecast skill of the ECMWF model depended on the sign of the PNA pattern. In particular, both Palmer (1988) and Molteni et al. (1990) pointed out that the −PNA is less predictable. The above results concerning the linear stability of the ±PNA patterns, based on normal mode growth, indicate differences with Molteni et al. (1990) and Palmer (1988). One difference between our results and those of Molteni and Palmer (1993) is that our PNA patterns are dynamically related to the atmospheric model because they minimize the tendency of the flow on the model attractor, while their PNA-like patterns were diagnosed statistically from data, thus without inherent dynamical relation to the model attractor. It is probable that the main difference between our results and the results of Palmer (1988) or Molteni and Palmer (1993) is due to the discrepancy between the observations and the models. This disagreement has been, and is still, observed. In fact, during the past decade or so, several studies have investigated the relationship between the winter atmospheric circulation and the SST anomaly variations in midlatitudes in both the North Atlantic and North Pacific. Various GCMs have been used to this end (e.g., Palmer and Sun 1985; Pitcher et al. 1988; Kushnir and Lau 1992) indicating contrasting results to the observational studies (Palmer and Sun 1985; Wallace and Jiang 1987) and indicating significant correlations between the 500-mb geopotential height and the SST anomaly in midlatitudes. Peng et al. (1995) pointed out that the major discrepancies observed in the previous studies could be caused by the use of different basic atmospheric conditions in the various experiments.

6. Summary and conclusions

In this paper, we started by reviewing the technique introduced in Part I to look for quasi-stationary states or weather regimes from a GCM. This method explores the dynamical properties of the 500-mb EOF phase space within which weather regimes were sought by minimizing the average streamfunction tendency, based on the barotropic vorticity equation, and giving rise to two states, namely ±PNA. These dynamical states were found in Part I to affect the model trajectory, based on a statistical mixture analysis technique.

The difference in the cost function minimum between the +PNA and the −PNA regimes has led us to study the flow tendency based on the barotropic vorticity equation within the EOF phase space, which shows a regular and smooth flow where the +PNA location appears to be an unstable node, while the −PNA region is a stable node with a flow transition from +PNA toward −PNA. This transition is found to require approximately 37 days on the basis of barotropic vorticity advection. This large period is mainly due to the averaging effect. The preceding observations have been investigated by studying the stability of the regimes using full normal modes and with the reduced EOF phase space, showing that, generally, the +PNA regime is more unstable than the −PNA. It has been, particularly, shown that the low *e*-folding time of the most

unstable disturbance mode of the +PNA within the phase space is related to the wave amplitude and localized structure of this pattern that is similar to blocking. The singular vector analysis also shows that the −PNA pattern might be more predictable than the +PNA pattern. It has been pointed out that there is a difference between our dynamical states that minimizes the field tendency within the model attractor and the regimes discussed in Molteni and Palmer (1993), for example, which might explain the difference with their results, although it is also possible that the difference with Palmer (1988) or Molteni and Palmer (1993) is due to the discrepancies between the observations and models (Palmer and Sun 1985).

The results reported in this paper show that the quasi-stationary states of the actual GCM model run, namely ±PNA, have different dynamical behavior where the +PNA seems to be more unstable and less predictable than the −PNA pattern. This helps in understanding some of the results concerning the diagnostics of the solutions in Part I and raises some interesting points concerning the predictability of the −PNA pattern. We speculate about the possibility of improving its predictability by periods of up to two weeks. This speculation needs, of course, further diagnostics on observed datasets.

Acknowledgments. This work was funded by the NERC under Grant GR3/8274. The 10-year run of the GCM was supported by UGAMP. The author is grateful to Dr. K. Haines for helpful discussions and improving the original manuscript and wishes to thank Drs. I. Held and J. Anderson for valuable discussions during a visit to GFDL, Dr. G. Branstator who helped in getting the barotropic normal mode package from NCAR, and three anonymous reviewers for their helpful comments that improved the manuscript.

REFERENCES

Anderson, J. L., 1992: Barotropic stationary states and persistent anomalies in the atmosphere. *J. Atmos. Sci.,* **49,** 1709–1722.

Andrews, D. G., 1984: On the stability of forced non-zonal flows. *Quart. J. Roy. Meteor. Soc.,* **110,** 657–662.

Borges, M. D., and P. D. Sardeshmukh, 1995: Barotropic Rossby wave dynamics of zonally varying upper-level flows during Northern Hemisphere winter. *J. Atmos. Sci.,* **52,** 3779–3796.

Branstator, G., 1987: A striking example of the atmosphere's leading traveling pattern. *J. Atmos. Sci.,* **44,** 2310–2323.

——, 1995: Organization of storm track anomalies by recurring low-frequency circulation anomalies. *J. Atmos Sci.,* **52,** 207–226.

——, and J. D. Opsteegh, 1989: Free solutions of the barotropic vorticity equation. *J. Atmos. Sci.,* **46,** 1799–1814.

Charney, J. G., and J. G. Devore, 1979: Multiple flow equilibria in the atmosphere and blocking. *J. Atmos. Sci.,* **36,** 1205–1216.

Dole, R. M., and N. M. Gordon, 1983: Persistent anomalies of the extratropical Northern Hemisphere wintertime circulation: Geographical distribution and regional persistence characteristics. *Mon Wea. Rev.,* **111,** 1567–1587.

Egger, J., 1978: Dynamics of blocking highs. *J. Atmos. Sci.,* **35,** 1788–1801.

Frederiksen, J. S., 1992: Towards a unified instability theory of large-scale atmospheric disturbances. *Trends Atmos. Sci.,* **1,** 239–261.

——, and R. C. Bell, 1990: North Atlantic blocking during January 1979: Linear theory. *Quart. J. Roy. Meteor. Soc.,* **116,** 1289–1313.

Haines, K., and A. Hannachi, 1995: Weather regimes in the Pacific from a GCM. *J. Atmos. Sci.,* **52,** 2444–2462.

Hansen, A. R., and A. Sutera, 1986: On the probability density distribution of large-scale atmospheric wave amplitude. *J. Atmos. Sci.,* **43,** 3250–3265.

Hoskins, B. J., and D. J. Karoly, 1981: The steady linear response of a spherical atmosphere to thermal and orographic forcing. *J. Atmos. Sci.,* **38,** 1179–1196.

——, I. N. James, and G. H. White, 1983: Shape, propagation, and mean-flow interaction of large scale weather systems. *J. Atmos. Sci.,* **40,** 1595–1612.

James, P. M., K. Fraedrich, and I. N. James, 1994: Wave–zonal flow interaction and ultra-low-frequency variability in a simplified global circulation model. *Quart. J. Roy. Meteor. Soc.,* **120,** 1045–1067.

Kimoto, M., M. Mukougawa, and S. Yoden, 1992: Medium-range forecast skill variation and blocking transition: A case study. *Mon. Wea. Rev.,* **120,** 1616–1627.

Kushnir, Y., and N. C. Lau, 1992: The general circulation model response to a North Pacific SST anomaly: Dependence on time scale and pattern polarity. *J. Climate,* **5,** 271–283.

Legras, B., and M. Ghil, 1985: Persistent anomalies, blocking, and variations in atmospheric predictability. *J. Atmos. Sci.,* **42,** 433–471.

Lorenz, E. N., 1963: Deterministic nonperiodic flow. *J. Atmos. Sci.,* **20,** 130–141.

——, 1965: A study of the predictability of a 28-variable atmospheric model. *Tellus,* **17,** 321–333.

——, 1985: The growth of errors in prediction. *Turbulence and Predictability in Geophysical Fluid Dynamics and Climate Dynamics,* M. Ghil, R. Benzi, and G. Parisi, Eds., North Holland, 243–265.

Mansfield, D. A., 1986: The skill of dynamical long-range forecasts, including the effect of sea surface temperature anomalies. *Quart. J. Roy. Meteor. Soc.,* **112,** 1145–1176.

Mo, K. C., and M. Ghil, 1988: Cluster analysis of multiple planetary flow regimes. *J. Geophys. Res.,* **93,** 927–952.

Molteni, F., and T. N Palmer, 1993: Predictability and finite-time instability of the northern winter circulation. *Quart. J. Roy. Meteor. Soc.,* **119,** 269–298.

——, S. Tibaldi, and T. N. Palmer, 1990: Regimes in the wintertime circulation over northern extratropics. I: Observational evidence. *Quart. J. Roy. Meteor. Soc.,* **116,** 31–67.

——, L. Ferranti, T. N. Palmer, and P. Viterbo, 1993: A dynamical interpretation of the global response to equatorial Pacific SST anomalies. *J. Climate,* **6,** 777–795.

Mukougawa, H., 1988: A dynamical model of ''quasi-stationary'' states in large-scale atmospheric motions. *J. Atmos. Sci.,* **45,** 2868–2888.

Namias, J., 1964: Seasonal persistence and recurrence of European blocking during 1958–1960. *Tellus,* **16,** 3.

Neven, E. C., 1993: Modons on a sphere. Ph.D. thesis, Rijksuniversiteit Utrecht, the Netherlands, 175 pp. [Available from E. C. Neven, Technische Universiteit Eindhoven, P.O. Box 513, 5600 MB Eindhoven, the Netherlands.]

Nitsche, G., J. M. Wallace, and C. Kooperberg, 1994: Is there evidence of multiple equilibria in planetary wave amplitude statistics? *J. Atmos. Sci.,* **51,** 314–322.

Palmer, T. N., 1988: Medium and extended range predictability and stability of the Pacific/North American mode. *Quart. J. Roy. Meteor. Soc.,* **114,** 691–713.

——, and Z. Sun, 1985: A modelling and observational study of the relationship between sea surface temperature in the north-west Atlantic and the atmospheric general circulation. *Quart. J. Roy. Meteor. Soc.,* **111,** 947–975.

——, and D. L. T. Anderson, 1994: The prospects for seasonal forecasting—A review paper. *Quart. J. Roy. Meteor. Soc.,* **120,** 755–793.

Peng, S., L. A. Mysak, H. Ritchie, J. Derome, and B. Dugas, 1995: The differences between early and midwinter atmospheric responses to sea surface temperature anomalies in the northwest Atlantic. *J. Climate,* **8,** 137–157.

Pitcher, E. J., M. L. Blackmon, G. T. Bates, and S. Munoz, 1988: The effect of North Pacific sea surface temperature anomalies on the January climate of a general circulation model. *J. Atmos. Sci.,* **45,** 173–188.

Quiroz, R. S., 1983: The climate of the ''El Niño'' winter of 1982/83—A season of extraordinary climatic anomalies. *Mon. Wea. Rev.,* **111,** 1685–1706.

Rasmusson, E. M., and J. M. Wallace, 1983: Meteorological aspects of the El Niño/Southern oscillation. *Science,* **222,** 1195–1202.

Rex, D., 1950: Blocking action in the middle troposphere and its effect upon regional climate. *Tellus,* **2,** 196–211.

Shutts, G. J., 1983: The propagation of eddies in diffluent jetstreams: Eddy vorticity forcing of blocking flow fields. *Quart. J. Roy. Meteor. Soc.,* **109,** 737–761.

Simmons, A. J., J. M. Wallace, and G. W. Branstator, 1983: Barotropic wave propagation and instability and atmospheric teleconnection patterns. *J. Atmos. Sci.,* **40,** 1363–1392.

Sutera, A., 1986: Probability density distribution of large-scale atmospheric flow. *Advances In Geophysics,* Vol. 29, Academic Press, 227–249.

Tung, K. K., and R. S. Lindzen, 1979: A theory of stationary long waves. Part I: A simple theory of blocking. *Mon. Wea. Rev.,* **107,** 714–734.

——, and A. J. Rosenthal, 1985: Theories of multiple equilibria—A critical reexamination. Part I: Barotropic models. *J. Atmos. Sci.,* **42,** 2804–2819.

Vautard, R., and B. Legras, 1988: On the source of low-frequency variability. Part II: Nonlinear equilibration of weather regimes. *J. Atmos. Sci.,* **45,** 2845–2867.

Verkley, W. T. M., 1989: On atmospheric blocking and the theory of modons. Ph.D. thesis, Free University, Amsterdam, the Netherlands, 171 pp. [Available from W. T. M. Verkley, Royal Netherlands Meterological Institute, P.O. Box 201, 3730 AE De Bilt, the Netherlands.]

Wallace, J. M., and D. S. Gutzler, 1981: Teleconnections in the geopotential height field during the Northern Hemisphere winter. *Mon. Wea. Rev.,* **109,** 784–812.

——, and Q. Jiang, 1987: On the observed structure of the interannual variability of the atmosphere/ocean climate system. *Atmospheric and Ocean Variability,* H. Cattle, Ed., Roy. Meteor. Soc., 17–43.